

Detailed study of the microwave emission of the supernova remnant 3C 396

A. Cruciani^{1,*}, E.S. Battistelli¹, E. Carretti^{2,3}, P. de Bernardis¹,
R. Genova-Santos^{4,5}, S. Masi¹, B. Mason⁶, D. Perera⁷, F. Piacentini¹,
B. Reach⁶, J.A. Rubino-Martin^{4,5}

¹*Department of Physics, Sapienza University of Rome, Piazzale Aldo Moro 5, 00185 Rome, Italy*

²*CSIRO Astronomy and Space Science, PO Box 276, Parkes, NSW 2870, Australia*

³*Cagliari Astronomical Observatory, Via della Scienza 5 - 09047 Selargius, CA, Italy*

⁴*Instituto de Astrofísica de Canarias, C/ Via Lactea, s/n, E38205, La Laguna, Tenerife, Spain*

⁵*Departamento de Astrofísica, Universidad de La Laguna (ULL), 38206 La Laguna, Tenerife, Spain*

⁶*National Radio Astronomy Observatory, 520 Edgemont Rd, Charlottesville, VA 22903*

⁷*National Radio Astronomy Observatory, P.O. Box 2, Green Bank, WV*

Received ...; accepted ...

ABSTRACT

We have observed the supernova remnant 3C 396 in the microwave region using the Parkes 64-m telescope. Observations have been made at 8.4 GHz, 13.5 GHz, and 18.6 GHz and in polarisation at 21.5 GHz. We have used data from several other observatories, including previously unpublished observations performed by the Green Bank Telescope at 31.2 GHz, to investigate the nature of the microwave emission of 3C 396. Results show a spectral energy distribution dominated by a single component power law emission with $\alpha = (-0.364 \pm 0.017)$. Data do not favour the presence of anomalous microwave emission coming from the source.

Polarised emission at 21.5 GHz is consistent with synchrotron-dominated emission. We present microwave maps and correlate them with infrared (IR) maps in order to characterise the interplay between thermal dust and microwave emission. IR vs. microwave TT plots reveal poor correlation between mid-infrared and microwave emission from the core of the source. On the other hand, a correlation is detected in the tail emission of the outer shell of 3C 396, which could be ascribed to Galactic contamination.

Key words: ISM: supernova remnants – ISM: individual objects: 3C 396 – radio continuum: ISM

1 INTRODUCTION

The nature of the emission of supernova remnants (SNRs) and their interaction with the surrounding medium can be studied with multifrequency observations ranging from the radio to the X-ray regions of the spectrum. In the microwave region, a detailed multifrequency analysis of SNR emission can shed light on the interplay between synchrotron emission, which typically dominates SNR radio emission, and the possible presence of other mechanisms such as anomalous microwave emission (AME, Draine & Lazarian (1998)). Of key importance is the ability to distinguish between different components within the emitting source as well as to disentangle local and foreground contaminants. To this end, high angular resolution (i.e. arcminute-level) observations

are crucial and allow one to distinguish different contributions within the same Galactic region (e.g. Battistelli et al. (2012)).

3C 396 is a shell-like SNR with a mean angular diameter of $7'.8$ (Patnaik et al. 1990). Its distance, estimated from *Chandra* data (Olbert et al. 2003) and updated by means of CO observations, is about 6.2 kpc, and its age is about 3000 yr (Su et al. 2011). Patnaik et al. (1990) performed a complete overview of the numerous radio observations of the source before 1990. Using high angular resolution observations at 1.4 GHz obtained with the Very Large Array (VLA), Patnaik et al. (1990) were able to identify the presence of two separate components in the source: the core, dominated by non-thermal synchrotron emission, and the tail, representing about 10% of the total flux at 1.4 GHz with a less steep spectral index compatible with free-free emission. Anderson and Rudnick (1993) discussed the spa-

* E-mail: angelo.cruciani@roma1.infn.it

tial spectral index variations of the spectral energy distribution (SED) in this SNR and concluded that these variations do not coincide with features in total intensity, but also found that the region associated with the brightest feature in the SNR has a somewhat flatter spectral index with respect to the average SNR spectral index. The presence of a small synchrotron pulsar wind nebula (PWN) within 3C 396 has been reported, although there is no spatial correspondence with the radio feature in high-resolution 20-cm VLA images of the remnant. This component could [would?] have a contribution of about 4% of the total radio flux density at 1.4 GHz (Olbert et al. 2003), not enough to explain the spatial spectral index variations of the SED in this SNR.

Scaife et al. (2007) observed 3C 396 with the Very Small Array (VSA) experiment (Watson et al. 2003) and tentatively reported finding anomalously high emission at 33 GHz, which suggested for the first time the possible presence of AME due to spinning dust in an SNR. As reported by Planck Collaboration (2015b), this evidence could not be confirmed by the *Planck* experiment owing to the lack of angular resolution and its vicinity to the Galactic plane. Besides AME, the excess seen by the VSA could also be explained by the presence of a significant level of thermal emission (about 50 % of the total emission at 1.4 GHz), causing the flattening of the spectrum at frequencies greater than 10 GHz (Onic et al. 2012). Scaife et al. (2007) emphasize the need for further measurements in the 10–20 GHz range, which is among the goals of the present paper.

An attempt to evaluate the amount of free-free emission was performed, using the radio recombination line (RRL) survey of the Galactic plane from the HI Parkes All-sky Survey (Alves et al. 2012, 2015); the presence of diffuse free-free emission in the 3C 396 region is quite evident, although the angular resolution is poor (beamwidth of 14.4 arcmin FWHM). A rough estimate of the total flux gives an upper limit of 3 Jy at 1.4 GHz.

Polarisation measurements of the SNR have been made, mainly at 5 GHz, and show the presence of a mean polarisation fraction of about 3% (Sun et al. 2011), with some regions being polarised at the 5–10% level and a small outer region being up to 50% polarised (Patnaik et al. 1990).

In this paper we present observations at arcminute-level resolutions of 3C 396 performed with the Parkes single-dish 64 m telescope at 8.4 GHz, 13.5 GHz, 18.6 GHz, and 21.5 GHz.

In Sections 2.1–2.4 we present the observations performed with the Parkes telescope, in Section 2.5 we introduce the previously-unpublished 3C 396 observations performed by the 100-m Green Bank Telescope (GBT) and in Section 3 we briefly introduce the remaining ancillary data used to fit the SED of the source. In Section 4 we study the morphology of the SNR and in Section 5 we present the SED, concentrating on the microwave band. The polarisation data, based on measurements at 21.5 GHz, are presented in Section 6. In Section 7 we show the correlation between IR and microwave data.

2 OBSERVATIONS AND DATA REDUCTION

Observations were made in four different frequency bands with the 64-m Parkes Radio Telescope, NSW Australia, op-

erated by ATNF-CASS, CSIRO: photometric observations were conducted at three frequencies (8.4 GHz, 13.5 GHz, and 18.6 GHz) and polarisation observations at 21.5 GHz. A further unpublished observation performed by GBT at 31.2 GHz is presented in the last subsection.

2.1 8.4 GHz observations

The 8.4 GHz observations were conducted with the MARS receiver of the Parkes telescope on 26 July 2011 for 4 h. The receiver is a circular polarisation system with $T_{\text{sys}} \sim 30$ K, a resolution of 2.4 arcmin, and a bandwidth of 400 MHz centred at 8.4 GHz. To measure the whole useful bandwidth the backend Digital Filter Banks Mark 3 (DFB3) was used with a configuration of 512 frequency channels of 2 MHz resolution for a total bandwidth of 1024 MHz. The correlator has full Stokes parameter capability, recording the two autocorrelation products RR^* , LL^* and the complex cross-product RL^* whose real and imaginary parts are the two Stokes parameters Q and U . The gain is 1.18 Jy K^{-1} . The source PKS B1934-638 was used for flux density scale calibration with an accuracy of 5% (Reynolds 1994).

The channels spanning the 400 MHz band were then binned into twenty 20-MHz sub-bands. A standard basket-weaving technique with two orthogonal scan sets along R.A. and Dec. spaced by 45 arcsec was used to observe an area of $20' \times 20'$ centred on the source. The scan speed was $0^\circ.5/\text{min}$, with a sampling time of 0.25 s. For each scan, a linear fit performed off-source is removed. Map-making software based on the Emerson & Grave (1988) Fourier algorithm was applied to make the maps (Carretti et al. 2010). This technique effectively reduces $1/f$ noise and removes stripes and features that differ between the two orthogonal sets of scans.

The twenty sub-band maps were binned together in one map for the analysis. The final rms on the map is 22 mJy/beam on a beam-size scale. This is higher than the expected sensitivity (~ 0.7 mJy/beam); however, 3C 396 is located at $(l, b) = (39^\circ.2, -0^\circ.3)$, close to the Galactic plane, and the excess signal could be due to diffuse Galactic emission. To investigate this possibility we analysed the 1.4 GHz CHIPASS map (Calabretta et al. 2014), which has a resolution of 14.5 arcmin, and found an rms of 650 mK in the area around 3C 396. Following (Battistelli et al. 2015) we estimate an rms from the Galactic signal at our frequency and resolution of 23 mJy/beam, quite consistent with the rms signal directly measured around the source in our map.

2.2 13.5 GHz observations

The 13.5 GHz observations were conducted with the Ku-band receiver of the Parkes telescope on 31 August 2011 and 1 September 2011, for a total of 3 h. The receiver is a linear polarisation package with $T_{\text{sys}} \sim 150$ K, a resolution of 1.7 arcmin, and a bandwidth of 700 MHz centred at 13.55 GHz. To detect the whole useful bandwidth the backend Digital Filter Banks Mark 3 (DFB3) was used with a configuration of 512 frequency channels of 2 MHz resolution for a total bandwidth of 1024 MHz. Only the two autocorrelation products were used (XX^* , YY^*) for Stokes I measurements. The gain is 1.55 Jy K^{-1} .

The source PKS B1934-638 was used for flux density

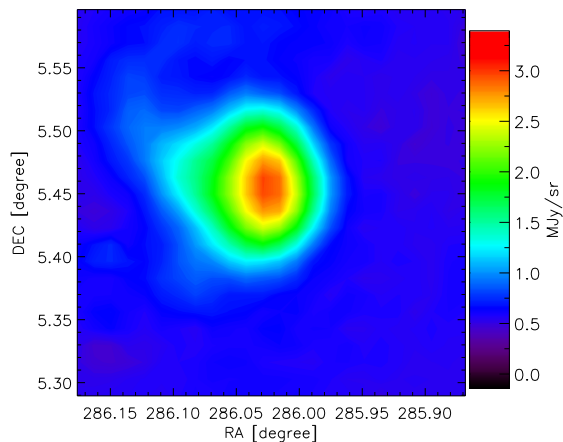


Figure 1. 8.4 GHz map of 3C 396 obtained with the Parkes Radio Telescope using the MARS receiver. The angular resolution is 2.4 arcmin (FWHM) and the final rms of the map is 22 mJy/beam (0.040 MJy/sr).

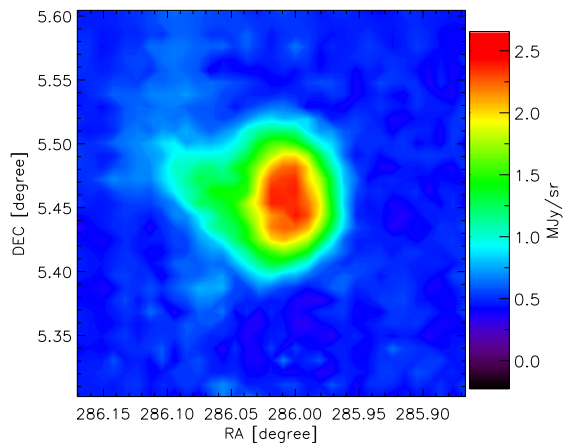


Figure 2. 13.5 GHz map of 3C 396 obtained with the Parkes Radio Telescope using the Ku-band receiver. The angular resolution is 1.7 arcmin (FWHM) and the final rms of the map is 18 mJy/beam (0.065 MJy/sr).

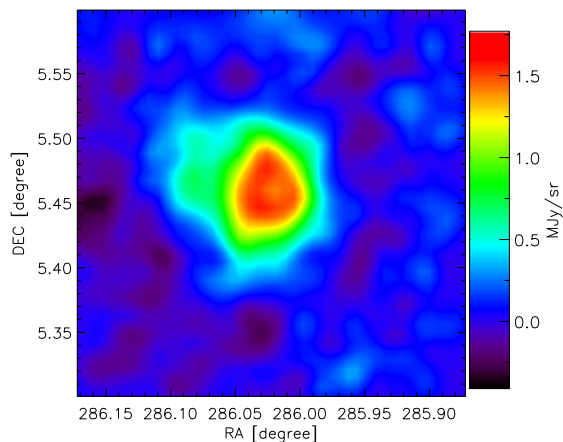


Figure 3. 18.6 GHz map of 3C 396 obtained with the Parkes Radio Telescope using the 13-mm receiver. The angular resolution (after smearing to Ku-band angular resolution) is 1.7 arcmin (FWHM) and the final rms of the map is 32 mJy/beam (0.11 MJy/sr).

scale calibration with an accuracy of 5% (Reynolds 1994). The atmospheric opacity when observing the calibrator was 0.085 dB at the observing elevation (EL); we correct for this attenuation in all our data. During the observations the opacity ranged from 0.074 to 0.120 dB (including EL effects) for a maximum variation compared to the constant opacity correction of 0.035 dB (0.8%), with marginal effects on the flux density scale accuracy. The opacity at zenith was computed from atmospheric parameters (temperature, pressure, and relative humidity) and used to compute the opacity at the observing elevation correcting for EL effects ($1/\cos(\text{EL})$).

The channels spanning the 700 MHz band were binned into seven 100-MHz sub-bands for the subsequent map-making processing. An area of $20' \times 20'$ centred at the source was observed with a standard basket-weaving pattern, in which we performed two orthogonal scan sets along R.A. and Dec. The scans were spaced by 30 arcsec, the scan speed was $0^\circ.5/\text{min}$, and the sampling time 0.25 s. After running the map-making software, the seven sub-band maps were co-added. The final rms signal on the map is 18 mJy/beam on beam-sized scales, larger than the expected sensitivity (4 mJy/beam). Following the same argument presented in Section 2.1 2.1, we estimate a Galactic emission contribution of $\text{rms}_{13.5 \text{ GHz}}^{1.7'} = 12 \text{ mJy/beam}$ at the frequency and resolution of our observations, consistent with the measured value.

2.3 18.6 GHz observations

The 18.6 GHz observations were conducted with the 13-mm receiver of the Parkes telescope on 29 August 2011 for a total of 3 h. This receiver can be set up either with a linear polarisation feed covering the frequency range 16–26 GHz or with a circular polariser covering 21.0–22.3 GHz. We used the linear polarisation configuration with a 800 MHz IF band centred at 18.6 GHz. The system temperature was $T_{\text{sys}} \sim 70 \text{ K}$, and the resolution was 76 arcsec. The backend DFB3 was used with a configuration of 512 frequency channels of 2 MHz resolution for a total bandwidth of 1024 MHz. Only the two autocorrelation products were used (XX^* , YY^*) for Stokes I measurements. The gain is 1.56 Jy K^{-1} .

The source PKS B1921-293 was used to calibrate the flux density scale with an assumed flux of 17.2 Jy, and accuracy of 10%. This is a variable source on a time scale of a few weeks and its flux density was measured with the Australia Telescope Compact Array the day after the Parkes observations (31 August 2011). The opacity when observing the calibrator was 0.19 dB at the observing elevation, and we corrected all our data for this attenuation. During the observations the opacity ranged from 0.18 to 0.28 dB (including EL effects) for a maximum variation compared to the constant opacity correction of 0.09 dB (2%), with marginal effects on the flux density scale accuracy.

The frequency channels spanning the 800 MHz band were binned into four 200-MHz sub-bands for the subsequent map-making step. An area of $20' \times 20'$ centred at the source was observed with a standard basket-weaving pattern, in which we performed two orthogonal scan sets along R.A. and Dec.

The scans were spaced by 24 arcsec, the scan speed was $0^\circ.5/\text{min}$, and the sampling time 0.25 s. The map-

making software was run and the four sub-band maps were co-added into a single map. We reached an rms sensitivity of 32 mJy/beam on beam-sized scales, after smearing the map to the angular resolution to the Ku-band observations, larger than the expected sensitivity (2 mJy/beam). As described in Section 2.1, we estimate a Galactic emission contribution of $\text{rms}_{18.6\text{ GHz}}^{1.7'} = 12$ mJy/beam at the frequency and final resolution of our map. This can only partly explain the rms signal excess we measure. Possible sources of the additional noise are atmospheric emission fluctuations or a $1/f$ -noise contribution from the receiver amplifiers. We do not have enough data to determine which of the two effects might have the greater contribution.

2.4 21.5 GHz observations

The 21.5 GHz observations were conducted with the 13 mm receiver of the Parkes telescope on 30 August 2011 for a total of 3 h. We used the circular polarisation set-up with a 900 MHz band centred at 21.55 GHz. The system temperature was $T_{\text{sys}} \sim 95$ K, and the resolution was 67 arcsec. The backend DFB3 was used with a configuration of 512 frequency channels of 2 MHz resolution for a total bandwidth of 1024 MHz. All autocorrelation and complex cross-products of the two circular polarisations were recorded (RR^* , LL^* , RL^*). The gain was 1.70 Jy K^{-1} . Observations consisted of 111 repeated scans of one strip through the source at fixed $\text{DEC} = 5^\circ.43$ from $\text{RA} = 285^\circ.90$ to $\text{RA} = 286^\circ.20$ and back.

The source PKS B1921-293 was used to calibrate the flux density scale with an assumed flux of 16.5 Jy, and accuracy of 10%. The opacity when observing the calibrator was 0.47 dB at the observing elevation, and all our data are corrected for this attenuation. During the observations the opacity ranged from 0.39 to 0.65 dB (including EL effects) for a maximum variation compared to the constant opacity correction of 0.19 dB (4%). Combined with the flux scale accuracy (10%) this gives a final accuracy of 11%.

Off-axis instrumental polarisation can be as high as 0.6% in single observations. Cancellation effects (e.g., Carretti et al. 2004; O’Dea et al. 2007) and the rotation of the parallactic angle during the execution of the scans reduces this effect when averaging scans taken at different parallactic angles. Following Battistelli et al (2015), we estimated a level of 0.2% after averaging all scans. Combining with the on-axis term, the overall systematic residual instrumental polarisation is estimated at 0.3%.

The frequency channels over the 900 MHz band were binned into 90 sub-bands for flux and instrumental polarisation calibration. All the sub-bands were then combined for the subsequent analysis. We reached a sensitivity per beam-sized pixel of $\sigma_{Q,U}^{21.5\text{ GHz}} = 0.2$ mJy/beam in polarisation, consistent with the expected value. The fluctuations in Stokes I are larger with an rms of 6.0 mJy/beam, consistent with the rms of the Galactic signal that, following the procedure of Section 2.1, is estimated to be $\text{rms}_{21.5\text{ GHz}}^{6.7''} = 5.2$ mJy/beam at the frequency and resolution of the observations. The longer exposure time allowed the $1/f$ and atmospheric noise terms to be reduced below the Galactic diffuse emission confusion, making the latter the leading term of the noise budget.

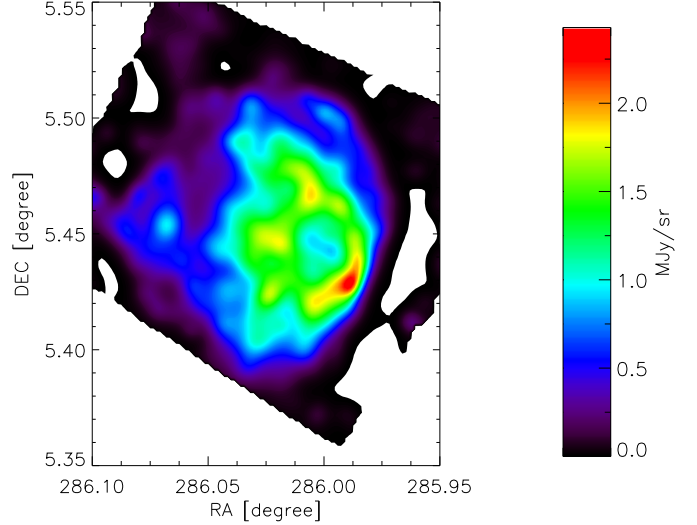


Figure 4. 31.2 GHz map of the core of 3C 396 obtained with the GBT Ka-band receiver. The angular resolution is 0.4 arcmin (FWHM).

2.5 Ka-band - Green Bank Telescope

A $\sim 9' \times 9'$ map of 3C 396 was made at 31.2 GHz under project AGBT10A-001 using the GBT Ka-band receiver (Jewell & Prestage 2004) and Caltech Continuum Backend (CCB).¹ The Ka-band receiver is a beam-switched pseudo-correlation receiver which, when used with the CCB, provides excellent continuum sensitivity; technical details of these systems are given in Mason et al. (2009). The GBT beam at 31 GHz is 24 arcsec (FWHM), and the two (differenced) beams read out by the CCB are separated by 78 arcsec in the cross-elevation direction on the sky. Data are calibrated using 3C 286, referenced to the *WMAP* absolute measurement of Jupiter (Weiland et al. 2011). There is a 15% calibration uncertainty, dominated by uncertainties in the overall beam area of the GBT. The sky map (see Figure 4) was estimated from the beam-switched data using a maximum entropy method (MEM) deconvolution (e.g., Cornwell et al. (1988) and Narayan et al. (1986)).

3 ANCILLARY DATA

Radio emission from 3C 396 has been investigated in depth in the past. We selected a number of previous observations, taking into consideration the quality, accuracy and angular resolution of the data. In Table 1 we show a summary of the data we used. When multiple observations are available, the flux at a given frequency is the weighted average of all the different measurements.

Patnaik et al. (1990) compiled a detailed list and analysis of the observations made before 1990. We include all these data. We were also able to retrieve the original map performed with the VLA at 1.468 GHz (with a beam FWHM of 54.4 arcsec and a noise rms of 16 mJy/beam) and at

¹ <http://www.astro.caltech.edu/~tjp/GBT/>.

4.860 GHz (with a beam FWHM of 16 arcsec and a noise rms of 2 mJy/beam), which will be used in the morphology section. In addition, we include more recent observations made with the Effelsberg telescope (Reich et al. 1997) as in Scaife et al. (2007). Recently, the SNR was observed at 5 GHz (in intensity and polarisation) by the Sino–German survey with the Urumqi telescope (Sun et al. 2011). The results are consistent with other observations in the literature at the same frequency. We analysed further observations at 8, 10, and 14 GHz (Langston et al. (2000), Handa et al. (1987)), which, however, were excluded owing to the low S/N ratio.

We also include the 33 GHz measurement presented in Scaife et al. (2007). Any comparison of data from Parkes and the Very Small Array (VSA) interferometer needs to take into account the different experiment architecture and their different sensitivities as a function of angular scale. A linear fit was subtracted from each linear scan in the Parkes observations to reduce atmospheric contamination and 1/f detector noise. Due to this procedure these maps are sensitive to angular scales roughly between the beam size and the map size (20 arcmin). The VSA observation was made in the extended configuration with a primary beam FWHM of ≈ 72 arcmin and a synthesized beam FWHM of ≈ 6 arcmin. (More details of the experimental set-up and data reduction can be found in Dickinson et al. (2004).) The VSA observation is more sensitive than the Parkes observation for scales between 20 and 72 arcmin, though Parkes has a finer angular resolution. In order to compare the same angular scales of in our two observations, each of which has a different window function, we reanalysed the VSA data. First, we filtered the VSA visibilities using the Parkes window function. Then, using standard AIPS (Greisen 1994) routines, we produced a sky map which we cleaned down to about 1.5 times the map noise sensitivity. In order to derive the flux densities of 3C 396 and the nearby HII region NRAO 591 simultaneously, we applied a double Gaussian fit. The resulting 3C 396 flux density is 5.20 ± 0.33 Jy. This value is lower than that derived in Scaife et al. (2007), 6.64 ± 0.33 Jy, as a consequence of the filtering process.

We also included in our analysis *Planck*-HFI observations between 100 and 853 GHz and *Herschel Space Observatory* data between 600 and 4300 GHz in order to properly characterise the contribution from thermal dust in the microwave region. *Planck*-LFI data of 3C 396 are not included owing to the lack of angular resolution and the vicinity to the Galactic plane (Planck Collaboration 2015b).

Planck DR2 maps (Planck Collaboration 2015a), downloaded from the Planck Legacy Archive,² were used to derive fluxes in the six frequency bands (100, 143, 217, 353, 545, and 857 GHz) of the High Frequency Instrument (HFI). These maps are supplied in the HEALPix pixelization (Gorski 2005) at a resolution of $N_{\text{side}} = 2048$. The fluxes shown in Table 1 were obtained within an aperture of radius $0^\circ.14$ centred at $(l, b) = (39^\circ.22, -0^\circ.31)$, after subtracting a median background level calculated in an external annulus between radii $0^\circ.14$ and $0^\circ.18$. Owing to the proximity of the Galactic plane, the uncertainties of these fluxes are dominated by background fluctuations rather than by instrumental noise. The flux uncertainties are estimated from

Table 1. Integrated fluxes used for the 3C 396 SED fit.

Frequency (GHz)	Flux (Jy)	Reference
0.160	35.9 ± 4.3	(a), (b)
0.408	27.0 ± 3.0	(c), (d)
0.750	18.2 ± 1.8	(e)
1.40	14.9 ± 1.3	(e), (f), (g), (h), (i), (l)
1.70	14.5 ± 0.8	(m)
2.70	10.9 ± 0.5	(g), (l), (n), (o), (p), (q), (r)
3.24	11.4 ± 0.7	(s)
4.87	8.5 ± 0.9	(t)
5.00	8.84 ± 0.53	(e), (g), (j), (k), (q), (u), (v)
6.63	10.2 ± 0.7	(s)
8.40	8.60 ± 0.43	This work
10.6	6.32 ± 0.8	(s)
13.5	6.30 ± 0.31	This work
18.6	4.0 ± 1.2	This work
33.0	$6.64(5.20) \pm 0.33$	This work (reviewed)
100	1.0 ± 3.1	This work
143	1.7 ± 3.7	This work
217	10 ± 14	This work
353	53 ± 61	This work
545	230 ± 210	This work
600	280 ± 150	This work
857	750 ± 650	This work
857	740 ± 380	This work
1200	1890 ± 780	This work
1874	2900 ± 1200	This work
4293	1500 ± 210	This work

(a)Dulk & Slee (1975) (b)Slee et al. (1977) (c)Shavers & Goss (1970)
(d)Fanti et al. (1974) (e)Kellermann et al. (1969) (f)Milne (1979)
(g)Altenhoff et al. (1970) (h)Shavers et al. (1976) (i)Patnaik et al. (1990)
(j)Reifenstein et al. (1970) (k)Sun et al. (2011) (l)Reich et al. (1997)
(m)Downes et al. (1981) (n)Milne et al. (1969) (o)Horton et al. (1969)
(p)Reich et al. (1984) (q)Gardner et al. (1975) (r)Day et al. (1970)
(s)Hughes & Butler (1969) (t)Altenhoff et al. (1978) (u)Binette et al.
(1981) (v)Milne & Dickel (1975) (w) Scaife et al. (2007)

the background fluctuations in the ring, taking into account the number of independent samples and the number of pixels in the aperture.

3C 396 was also observed by the *Herschel Space Observatory* during the project *Herschel* infrared Galactic Plane Survey (Hi-GAL) (Molinari et al. 2010). We derive flux in five bands (600, 857, 1200, 1870, and 4300 GHz), processing the data as in Traficante et al. (2011). The fluxes were calculated using aperture photometry in the same manner as the *Planck* HFI case described above. In order to calculate the uncertainty, which is dominated by background fluctuations, we split the annulus used to subtract the background in ten radial sub-rings and calculated the dispersion of the recovered fluxes using this ensemble of sub-rings. *Planck* and *Herschel* flux estimates are strongly affected by the foreground emission evident in their maps. This makes them only tentative detections and could be interpreted as upper limits of the mm and sub-mm emission from 3C 396 SNR.

4 MORPHOLOGY

3C 396 has a complex morphology that makes it difficult to determine the nature of its observed emission. The SNR is a shell-type object with highly non-uniform emission, and

² <http://pla.esac.esa.int/pla/>

Patnaik et al. (1990) observed the presence of a tail at $RA \simeq 286^{\circ}.07$, $DEC \simeq 5^{\circ}.47$ that accounts for about 10% of total integrated flux at 1.4 GHz. The tail emanates from the eastern side of the remnant and curves more than 120° before falling below detectability. Parkes measurements have been able – for the first time in the microwave – to partially resolve the structure of the SNR and its tail. A rough estimate of its contribution at the observed frequencies (8.4, 13.5 and 18.6 GHz) yields 10–20% of the total integrated flux. Using a TT-plot with the VLA 1.4 GHz VLA map and Parkes 13.5 GHz Parkes map and together with the definition of tail shown in Fig. 8, we find a spectral index for the tail of $(-0.16 \pm 0.02(stat) \pm 0.05(cal))$. This is compatible with free-free emission, as previously suggested by Patnaik et al. (1990).

In order to investigate the nature and the spatial properties of the emission, we made a spectral index map (Figure 5) from the two maps with highest angular resolution (VLA at 4.8 GHz and GBT at 31.2 GHz). The two maps were degraded to the same angular resolution and the spectral index was derived pixel-by-pixel using the relation $f(\nu) = k\nu^{-\alpha}$. The data at both frequencies have a high S/N ratio, and so the error in the fitting procedure is dominated by systematic errors (e.g., calibration error). This map is useful for investigating variations in the spectral index within the source itself: it exhibits a steeper spectral index ($-0.6 < \alpha < -0.4$) in the outer part of the core than in the inner part, where α is between -0.4 and -0.3 . This confirms claims by Anderson and Rudnick (1993) from data at 1.4 and 5 GHz.

The observation of such spectral variations in shell remnants can be associated with spatially-dependent particle acceleration or bends in the relativistic electron energy spectrum. We cannot exclude the possibility, however, that these variations are caused by free-free presence within the source, as suggested by Onic et al. (2012), or along the line of sight.

Analysis of the IR and sub-mm maps (see Fig. 9) retrieved from the *Herschel* and *SPITZER* experiments and ranging from $500 \mu\text{m}$ to $24 \mu\text{m}$ shows a lack of emission towards the core of 3C 396, while there is evidence of emission in the surrounding area, especially around the tail where the emission peaks at around $160 \mu\text{m}$. It should be stressed, however, that the closeness of the source to the Galactic plane makes its emission at all wavelengths fairly contaminated by the Galactic plane itself. It is therefore difficult to disentangle local and diffuse emission. A cross-correlation analysis between IR and microwave emission is performed in section 7.

5 SPECTRAL ENERGY DISTRIBUTION

In order to retrieve information about the overall emission of 3C 396 we have studied the SED of the SNR. To compare fluxes from all our available data, we reduced the maps in the same way: aperture photometry was performed with a radius of 8.5 arcmin after subtracting a background measured in an annulus with inner radius of 8.5 arcmin and outer radius of 10 arcmin. Reported errors are the combination of calibration error and map noise, estimated from background fluctuations.

Our baseline model of the SED has one power law com-

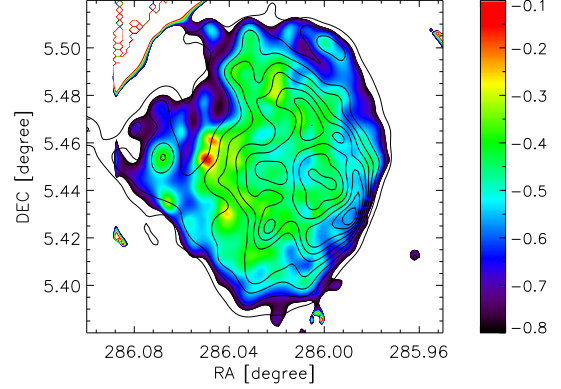


Figure 5. Spectral index map of 3C 396 calculated using the 4.8 GHz VLA map (beam FWHM of 16 arcsec) and the 31.2 GHz GBT map (beam FWHM of 25 arcsec). Contour levels are from the 31.2 GHz map and are at 0.23, 0.46, 0.68, 0.91, 1.14, 1.37, 1.59, 1.82, 2.05 and 2.28 MJy/sr.

ponent, S_y , and a thermal dust emission. Millimetre, sub-millimetre and FIR emission is clearly dominated by thermal dust emission, which we modelled as modified blackbody emission with fixed dust emissivity spectral index $\beta = 1.6$ (Planck Collaboration 2014a) and free parameters for the temperature T_d and the optical depth at $100 \mu\text{m}$, τ_{100} . The resulting model, which we fit with a routine based on the IDL MPFIT one Markwardt (2009), is therefore:

$$S(\nu) = S_y \cdot \nu^{\alpha_1} + \tau_{100} \left(\frac{\nu}{3\text{THz}} \right)^{\beta} \cdot BB_{\nu}(T_d) \Omega \quad (1)$$

where BB_{ν} is the Blackbody brightness and Ω is the total solid angle of the source. Results are shown in Figure 6. The SED of 3C 396 is well-described in the 1–30 GHz range Crab-like synchrotron component with $\alpha = (-0.364 \pm 0.017)$. The dust temperature is (25.1 ± 1.2) K and τ_{100} is $(3.6 \pm 1.2)10^{-4}$. The fit has χ -square = 24.6 (DOF=21).

We also tested more complex models by adding AME, using a fiducial model derived from Draine & Lazarian (1998), or including contaminations from free-free or a second power law component. To select the best model, we used the Akaike information criterion (AIC, Akaike et al. (1974); Burnham et al. (2002)), in which $AIC = 2k - \chi^2$, where k is the number of estimated parameters. These three modified models ($AIC \approx 34.5$) are all rejected by AIC with respect to the baseline model ($AIC \approx 32.5$).

We used the high angular resolution maps of VLA, Parkes and GBT to make a further SED fit restricted only to the core of 3C 396. Its flux was estimated from aperture photometry with a radius of 4.5 arcmin and background subtraction in an annulus with inner radius of 4.5 arcmin and outer radius of 6 arcmin (excluding the tail region). We obtain $\alpha = (-0.466 \pm 0.024)$ and find no anomalous emission.

Infrared and mm-wave measurements can constrain the contribution from dust at the frequencies where AME should be dominant (i.e., below 100 GHz). However, it is important to stress that 3C 396 is not unambiguously detected in these maps. Consequently the estimated fluxes can only be taken as upper limits on the SNR emission.

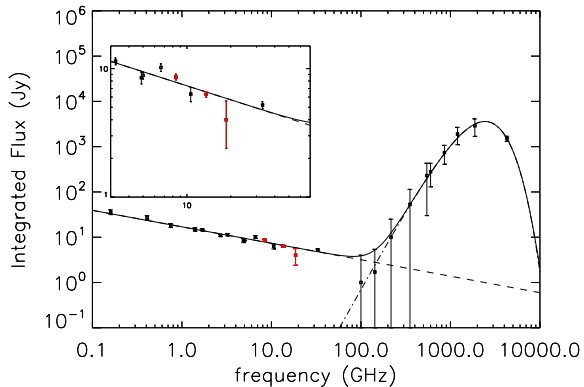


Figure 6. SED of 3C 396 including Parkes (in red) and the reprocessed VSA flux at 33 GHz. The fit indicates that one synchrotron component is the best explanation of the SED behaviour in the microwave range. The fit does not favour the presence of any spinning dust component or further power law components (e.g., free-free).

6 POLARISATION

Polarisation-sensitive observations at the fixed declination of $5^{\circ}26'6''$ were conducted at 21.5 GHz with the 13 mm receiver of the Parkes telescope. In Figure 7 we show the percentage polarised emission obtained from the combination of our one-dimensional scans. Only the polarisation fraction is presented since the measurements are affected by gain fluctuations on long time scales (> 6 hrs) and cannot be reliably calibrated. As previously described, spurious polarisation and depolarisation are verified to be less than 0.3%. Any estimate of polarised intensity (PI), and consequently of polarisation fraction, is intrinsically overestimated unless a debiasing procedure is applied (Wardle & Kronberg (1974)). For this reason, we adopted a debiasing procedure described in Battistelli et al. (2015), which is based on the Bayesian approach of Vaillancourt (2006). For high signal-to-noise data ($PI/\sigma > 5$), we set a debiased polarised intensity of $\sqrt{(PI^2 - \sigma^2)}$ as suggested by Wardle & Kronberg (1974). Some of our polarised measurements are in the low signal-to-noise regime in which the debiasing is particularly complex. For $PI/\sigma < 2$ we set upper limits, while in the intermediate range we integrate the posterior probability density function over the parameter space of the true polarisation.

We detect a polarisation of about 5 % in the outer regions of the source, while in the core values are lower (1–4 %). These results are in good agreement with previous measurements at 5 GHz (Patnaik et al. (1990), Sun et al. (2011)). Sun et al. (2011) observed a mean polarisation in the same one-dimensional scan of the source of $(2.4 \pm 0.4)\%$, which is compatible with our average measurement of $(2.4 \pm 0.1(\text{rand}) \pm 0.3(\text{sys}))\%$. This result seems to discount the possibility of a large amount of free-free emission at 1 GHz (of about 40%) as suggested by Onic et al. (2012), since one that would require the polarisation at 21.5 GHz to be about half of that at 5 GHz. Further, we can assume that the nature of 3C 396 emission does not dramatically change from radio to microwave frequencies.

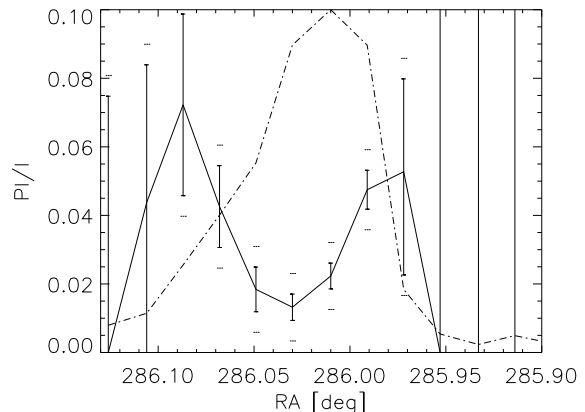


Figure 7. Observation of the fraction of polarised intensity over the total intensity at 21.5 GHz (fixed declination $\text{DEC}=5^{\circ}.43$), observed with Parkes. Error bars are quoted at the 2σ level. The dot-dashed line is the profile of the total intensity emission of the source at 21.5 GHz in arbitrary units.

7 INFRARED CORRELATION

Studying the possible spatial correlations between our microwave data and IR data is of interest since the correlation between AME and thermal dust emission is well known (e.g. Davies et al. (2006), Vidal et al. (2007), Dickinson et al. (2007), Todorovic et al. (2010), Génova-Santos et al. (2011), Tibbs et al. (2012), Dickinson (2013)). In the case of 3C 396 any correlation between our microwave data and IR data would hint at the presence of AME below the detection limit.

The region emissivity is usually defined as the ratio between the source emission at a frequency near the spinning dust peak (~ 20 – 30 GHz) and the FIR signals at $100 \mu\text{m}$. Dickinson (2013) reports HII region emissivity in units of $\mu\text{K}/(\text{MJy}/\text{sr})$ for microwave emission in the range 10 to 70 GHz relative to IRAS $100 \mu\text{m}$. These show emissivities of the same order of magnitude as high latitude diffuse cirrus (i.e., $\sim 10 \mu\text{K}/(\text{MJy}/\text{sr})$), though it is significantly lower in some regions. Pixel-by-pixel correlations measured by Vidal et al. (2007) in ρ Ophiuchi and LDN1780 show a clear correlation with a trend favouring the short wavelengths IR bands (i.e., $60 \mu\text{m}$ and $25 \mu\text{m}$). Recently, the *Planck* experiment studied all-sky correlations, showing an excellent correlation (Pearson $r = 0.98$) with the map at 545 GHz and an average emissivity of about $70 \mu\text{K}/(\text{MJy}/\text{sr})$ (Planck Collaboration 2015c). The analysis of selected known AME sources has significant correlation (Pearson $r > 0.6$) and similar values of emissivity.

In order to compare our microwave measurements with IR emission, we make use of the SPIRE, PACS and MIPS IR maps from the *Herschel* (Molinari et al. 2010) and *SPITZER* (Rieke et al. 2004) experiments, ranging from $500 \mu\text{m}$ to $24 \mu\text{m}$. In Figure 9 we compare the Parkes Ku 13.5 GHz map with those extracted from the SPIRE instrument ($500 \mu\text{m}$) and the PACS instrument ($160 \mu\text{m}$ and $70 \mu\text{m}$) after smoothing them to the angular resolution of the Parkes 13.5 GHz band. 3C 396 has been divided into two regions (tail and core), as shown in Fig-

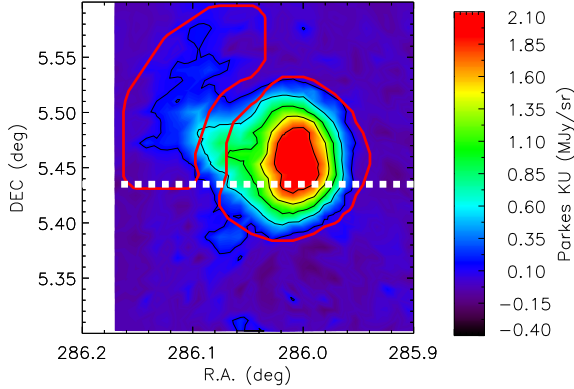


Figure 8. Parkes 13.5 GHz map of 3C 396 with superimposed indications of our region selection and the polarisation scan path. In order to perform a meaningful correlation analysis and to obtain the TT-plots shown in Figure 7, we have divided 3C 396 source into two regions, one covering the core (central elliptical contour) and one covering the tail (lateral semicircular contour). The white dashed line illustrates the path of the polarisation scan reported in Figure 7. Contour levels, from the 13.5 GHz map, are at 0.2, 0.70, 1.2, 1.70, and 2.2 MJy/sr.

ure 8. A lack of FIR emission is evident towards the core region of 3C 396, whereas there are bright FIR structures towards the northeast, where the tail identified by Patnaik et al. (1990) and also hinted at in our Parkes data is located. These FIR structures have been studied in different publications (Reach et al. (2006), Lee et al. (2009), Andersen et al. (2011)).

In the three right panels of Figure 9 we show TT correlation plots between the FIR and the radio emission at 13.5 GHz from Parkes. A significant correlation is evident between the data sets for the tail region, whereas for the core region we see possible anti-correlation or no correlation at all.

Pearson correlation coefficients for the tail emission are reported in Table 2. The statistical significance is at the 0.2% level and we make significant measurements of all the coefficients. The slope of a linear fit to the pixels defining the tail-region gives an estimate of the emissivity in the range 70–3500 $\mu\text{K}/(\text{MJy sr}^{-1})$. These values are considerably higher than what was found for typical AME and HII regions. The correlation coefficient R between 13.5 GHz Parkes map and the 500 μm map is lower than typical values estimated by the *Planck* experiment. Moreover, a close comparison between the IR maps and the microwave maps does not allow us to exclude the possibility that the IR emission is unassociated with the SNR and its microwave emission.

8 CONCLUSIONS

We have performed new intensity observations of the SNR 3C 396 with the Parkes telescope at 8.4, 13.5, and 18.6 GHz and analysed them together with unpublished 31.2 GHz data from the GBT telescope. We have calculated the SED of the core of the source and its surroundings. Our observations argue against the presence of an AME component

Table 2. Results of the correlation analysis of tail emission between 13.5 GHz and IR experiments

Instrument	Pearson	slope	slope ($\mu\text{K}/(\text{MJy}/\text{sr})$)
SPITZER 24	0.369	$(1.15 \pm 0.23) \times 10^{-2}$	2050 ± 410
PACS 70	0.674	$(1.13 \pm 0.10) \times 10^{-3}$	202 ± 17
PACS 160	0.574	$(3.36 \pm 0.38) \times 10^{-4}$	60 ± 10
SPIRE 250	0.537	$(4.67 \pm 0.58) \times 10^{-4}$	83 ± 11
SPIRE 350	0.504	$(9.9 \pm 1.4) \times 10^{-4}$	180 ± 25
SPIRE 500	0.480	$(2.37 \pm 0.34) \times 10^{-3}$	420 ± 60

from the core of the source. When accounting for the surrounding region, the SED is well-described by a power law with a Crab-like spectral index. We find a spatial spectral index variation between 5 GHz and 31.2 GHz that is consistent with the variation reported by Anderson and Rudnick (1993) between 1.4 GHz and 5 GHz.

We have also performed new polarisation observations at 21.5 GHz that seem to confirm that 3C 396 emission is dominated by synchrotron, without any important contamination due to free-free as suggested by Onic et al. (2012).

The absence of correlation between IR and 13.5 GHz emission in the core of 3C 396 is a further finding, confirming that the emission of 3C 396 is not anomalous. On the other hand, we find a significant correlation in the tail-region at short wavelengths (i.e., $< 160 \mu\text{m}$), as in other AME sources; however, this is probably due to diffuse emission from the Galactic plane.

ACKNOWLEDGMENTS

We acknowledge the logistic support provided by Parkes operators. The Parkes radio telescope is part of the Australia Telescope National Facility, which is funded by the Commonwealth of Australia for operation as a National Facility managed by CSIRO. The American National Radio Astronomy Observatory is a facility of the National Science Foundation operated under cooperative agreement by Associated Universities, Inc. We would like to thank A.D. Hincks, M. Hobson, A. Scaife for useful suggestions and comments. We thank the referee for providing constructive comments and help in improving the contents of this paper.

REFERENCES

- Akaike, H. 1974, IEEE Trans. on Automatic Control, 19, 716 (1974)
- Altenhoff, W. J. et al. 1970, A&AS, 1, 319 (1970)
- Altenhoff, W. J. et al. 1978, Astron. Astrophys. Suppl., 35, 23 (1978)
- Alves, M.I.R., et al. 2012, MNRAS 422,2429 (2012)
- Alves, M.I.R., et al. 2015, MNRAS 450,2025 (2015)
- AMI Consortium: Scaife A. M. M. et al. 2009, MNRAS, 394, L46 (2009)
- Andersen, M. et al. 2011, ApJ, 742, 7 (2011)
- Anderson, M. C. and Rudnick, L., ApJ, 408, 514 (1993)
- Battistelli, E. S. et al. 2006, ApJ, 645, L141 (2006)

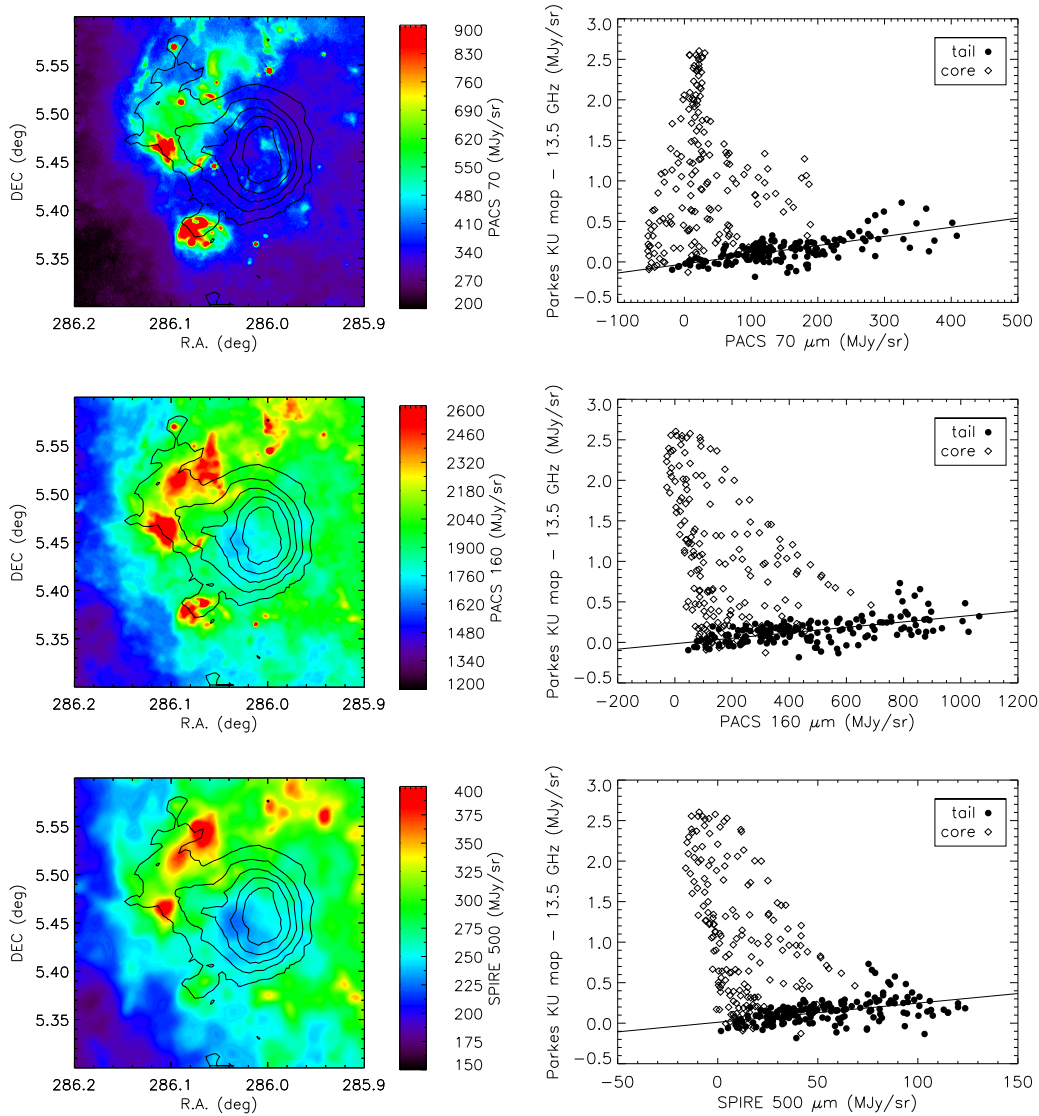


Figure 9. Left column from top to bottom: 13.5 GHz Parkes map (contours) vs. Pacs 70 μm , Pacs 160 μm , and SPIRE 500 μm maps. The right column has the corresponding scatter plots, i.e., microwave map vs IR map. White diamonds denote emission from the core of 3C 396 while black circles denote that of the tail, with the definition of these two regions shown in Figure 8. Contour levels, from the 13.5 GHz map, are at 0.2, 0.70, 1.2, 1.70, and 2.2 MJy/sr.

Battistelli, E. S. et al. 2012, *Advances in Astronomy*, 645, L141 (2012)
 Battistelli, E. S. et al. 2015, *ApJ*, 801, 111 (2015)
 Binette, L. et al. 1981, *Aust. J. Phys.*, 34, 407 (1981)
 Burnham, K. P. et al. 2002, Springer-Verlag, ISBN 0-387-95364-7.
 Calabretta M.R., Staveley-Smith L., Barnes D.G., 2014, *PASA*, 31, 7 (2014)
 Carretti E., et al., 2004, *A&A* 420, 437 (2004)
 Carretti E. et al. 2010, *MNRAS*, 405, 1670 (2010)
 Casassus, S. et al. 2008, *MNRAS*, 391, 1075 (2008)
 Castellanos, P. et al. 2011, *MNRAS*, 411, 2, 1137 (2011)
 Cornwell, T.J., *A&A*, 202, 316 (1988)
 Davies, R.D. et al. 2006, *MNRAS*, 370, 1152-1139 (2006)
 Day, G.A. et al. 1970, *Aust. J. Phys. Suppl.*, 13, 11 (1970)
 de Oliveira-Costa, A. et al. 1997, *ApJ*, 482, L17 (1997)

Dickinson, C., *Advances in Astronomy*, 162478 (2013)
 Dickinson, C., Battye, R.A., Carreira, P., et al., *MNRAS*, 353, 732 (2004)
 Dickinson, C. et al. 2007, *MNRAS*, 379, 297 (2007)
 Dickinson, C., et al., et al. 2009, *ApJ*, 690, 1585 (2009)
 Draine, B. T. & Lazarian, A. 1998, *ApJ*, 494, L19 (1998)
 Downes, A.J.B. et al. 1981, *Astron. Astrophys.*, 97, 296 (1981)
 Dulk, G.A. & Slee, O.B. 1975, *ApJ*, 199, 61 (1975)
 Emerson D.T., Gräve R., 1988, *A&A*, 190, 353 (1988)
 Fanti, C. et al. 1974, *Astron. Astrophys. Suppl.*, 16, 43 (1974)
 Finkbeiner, D. P. et al. 2004, *ApJ*, 617, 350 (2004)
 Gardner, F.F. et al. 1975, *Aust. J. Phys. Suppl.*, 35, 1 (1975)
 Génova-Santos, R. et al. 2011, *ApJ*, 743, 67 (2011)

- Ghosh, T. et al. 2012, MNRAS, 422, 3617 (2012)
- Górski, K.M., Hivon, E., Banday, A.J., et al., APJ, 622, 759 (2005)
- Greisen E., AIPS Cookbook. NRAO, Green Bank, WV (1994)
- Handa, T. et al. 1987, PASJ, 39, 709 (1987)
- Haynes, R. F. et al. 1978, Aust. J. Phys. Astrophys. Suppl., 45, 1 (1978)
- Hildebrandt, S. R. et al. 2007, MNRAS, 382, 594-608 (2007)
- Horton, P.W. et al. 1969, MNRAS, 143, 245 (1969)
- Hughes, V.A. & Butler, R. 1969, ApJ, 155, 1061 (1969)
- SPIE proceedings, 5489, 312-313 (2004)
- Kellermann, K.I., et al. 1969, ApJ, 157, 1 (1969)
- Langston, G. et al. 2000, AJ, 119, 2801 (2000)
- Lee, H.-G. et al. 2009, ApJ, 691, 1042 (2009)
- Mason, B. S. et al. 2009, ApJ, 704, 1443 (2009)
- Markwardt, C. B. 2009, ASPCS, 411, 251 (2009)
- Milne, D. K. et al. 1969, Astrophys. Lett., 4, 121 (1969)
- Milne, D. K. & Dickel J.R. 1975, Aust. J. Phys., 28, 209 (1975)
- Milne, D. K. 1979, Aust. J. Phys., 32, 83 (1979)
- Molinari, S. et al., Pub. Astron. Soc. Pac., 122, 314 (2010)
- Narayan, R. & Nityananda, R., Ann. Rev. A & A 24, 127 (1986)
- O'Dea D., Challinor A., Johnson B. R., 2007, MNRAS, 376, 1767 (2007)
- Olbert, C.M., et al. 2003, ApJ 592,L45 (2003)
- Onic, D. et al. 2012, ApJ, 756, 61 (2012)
- Patnaik, A. R. et al. 1990, A&AS, 232, 467 (1990)
- Planck Collaboration, A&A 571, AA11 (2014)
- Planck Collaboration, A&A submitted (2015) arXiv:1502.01582 (2015a)
- Planck Collaboration, A&A submitted (2015), astro-ph:1409.5746 (2015b)
- Planck Collaboration, A&A submitted (2015), astro-ph:1506.06660 (2015c)
- Reach, W. T. et al. 2006, AJ, 131, 1479 (2006)
- Reich, W. 1982, A&AS, 48, 219 (1982)
- Reich, W. et al. 1984, Astron. Astrophys. Suppl., 58, 197 (1984)
- Reich, W., et al. 1990, A&AS, 85, 633 (1990a)
- Reich, W., et al. 1990, A&AS, 83, 539 (1990b)
- Reich P., Reich W., Fuerst E., 1997, A&AS, 126, 413 (1997)
- Reifenstein, E.C., et al. 1970, Astron. Astrophys, 4, 357 (1970)
- Reynolds J.E., 1994, ATNF Tech. Doc. Ser. 39.3040 (1994)
- Rieke, G., et al., 2004, ApJS, 154, 25 (2004)
- Scaife, A. et al. 2007, MNRAS, 377, L69 (2007)
- Sharpless, S. 1959, ApJS, 4, 257 (1959)
- Shavers, P.A. & Goss, W.M., 1970, Aust. J. Phys. Suppl., 14, 133 (1970)
- Shavers, P.A. et al. 1976, Astron. Astrophys., 53, 273 (1976)
- Sun, X.H., et al. 2011, A&A 536,A83 (2011)
- Tibbs, C. 2012, ApJ, 754:94, (2012)
- Todorovic, M. 2010, MNRAS, 406, 1629-1643 (2010)
- Vaillancourt, J.E. , PASP, 118, 1340 (2006)
- Vidal, M. et al., MNRAS, 414, 2424-2435 (2007)
- Wardle, J.F.C. and Kronberg, P.P., APJ, 194, 249 (1974)
- Watson, R. A. et al. 2003, MNRAS, 341, 1057 (2002)
- Scaife, A. et al. 2007, MNRAS, 377, L69-L73 (2007)
- Slee, O.B. 1977, Aust. J. Phys. Suppl., 43, 1 (1977)
- Su, Y., et al. 2011, ApJ, 727, 43 (2011)
- Traficante, a. et al., MNRAS, 416, 2932 (2011)
- Vidal, M. et al. 2011, MNRAS, 414, 2424 (2011)
- Ysard, N. et al. 2011, A&A, 535, 89 (2011)
- Weiland, J.L. et al. 2011, APJS 192, 19 (2011)